

RESEARCH ARTICLE

10.1002/2014JD021662

Key Points:

- An isotope data assimilation system was developed
- Vapor isotopes have the potential to constrain atmospheric dynamical fields
- More data from both satellite retrievals and in situ networks are necessary

Correspondence to:

K. Yoshimura,
kei@aori.u-tokyo.ac.jp

Citation:

Yoshimura, K., T. Miyoshi, and M. Kanamitsu (2014), Observation system simulation experiments using water vapor isotope information, *J. Geophys. Res. Atmos.*, 119, doi:10.1002/2014JD021662.

Received 17 FEB 2014

Accepted 9 JUN 2014

Accepted article online 12 JUN 2014

Observation system simulation experiments using water vapor isotope information

Kei Yoshimura^{1,2}, Takemasa Miyoshi^{3,4}, and Masao Kanamitsu^{5,6}

¹Atmosphere and Ocean Research Institute, University of Tokyo, Kashiwa, Chiba, Japan, ²Institute of Industrial Science, University of Tokyo, Kashiwa, Chiba, Japan, ³RIKEN Advanced Institute for Computational Science, Kobe, Japan, ⁴University of Maryland, College Park, Maryland, USA, ⁵Scripps Institution of Oceanography, UCSD, La Jolla, California, USA, ⁶Deceased 17 August 2011

Abstract Measurements of water vapor isotopes ($\delta^{18}\text{O}$ and δD) have dramatically increased in recent years with the availability of new spectroscopic technology. To utilize these data more efficiently, this study first developed a new data assimilation system using a local transform ensemble Kalman filter (LETKF) and the Isotope-incorporated Global Spectral Model (IsoGSM). An observation system simulation experiment (OSSE) was then conducted. The OSSE used a synthetic data set of vapor isotope measurements, mimicking Tropospheric Emission Spectrometer (TES)-retrieved δD from the mid-troposphere, SCanning Imaging Absorption spectroMeter for Atmospheric CHartographY (SCIAMACHY)-retrieved δD from the water vapor column, and the virtual Global Network of Isotopes in Precipitation (GNIP)-like surface vapor isotope (both δD and $\delta^{18}\text{O}$) monitoring network. For TES and SCIAMACHY, we assumed a similar spatiotemporal coverage as that of the real data sets. For the virtual GNIP-like network, we assumed ~200 sites worldwide and 6-hourly measurements. An OSSE with 20 ensemble members was then conducted for January 2006. The results showed a significant improvement in not only the vapor isotopic field but also meteorological fields, such as wind speed, temperature, surface pressure, and humidity, when compared with a test with no observations. For surface air temperature, the global root mean square error has dropped by 10%, with 40–60% of the decrease occurring in the east-southeast Asia where the concentration of observations is relatively higher. When there is a conventional radiosonde network, the improvement gained by adding isotopic measurements was small but positive for all variables.

1. Introduction

Because stable oxygen and hydrogen isotopes in water (H_2^{18}O and HDO) are sensitive to the phase changes of water during circulation, they are useful tracers for atmospheric water vapor cycling processes at various scales, such as large-scale transport [e.g., Dansgaard, 1964; Yoshimura et al., 2004] and cloud-related processes [e.g., Webster and Heymsfield, 2003; Worden et al., 2007]. The relation between atmospheric processes and isotopic information in water vapor and precipitation has therefore been studied intensively [e.g., Craig and Gordon, 1965; Ehrlert, 1974; Jouzel, 1986; Gedzelman and Arnold, 1994; Gat, 2000].

Unfortunately, there is a much smaller volume of isotopic observation data compared to more “traditional” meteorological data (e.g., wind, water vapor, precipitation, and temperature), which has greatly limited progress. For example, there are few observations of isotopes in precipitation over oceans, and even over land, observations of isotopes in precipitation at time scales shorter than a month are severely lacking. Moreover, until recently, it has been simply too expensive to observe vapor isotopes. Therefore, it has been difficult to produce isotopic distribution maps with global coverage at fine temporal and spatial resolutions. Simple interpolation or statistical regression methods have been used to estimate isotopic distributions from the available information [Bowen and Revenaugh, 2003; Bowen, 2008]. In contrast, distributions of the “traditional” meteorological variables have been made at fine scales for many years using objective analysis methods such as data assimilation, for use in numerical weather prediction.

Isotope-incorporated atmospheric general circulation models (AGCM) [Joussaume et al., 1984; Jouzel et al., 1987; Hoffmann et al., 1998; Mathieu et al., 2002; Noone and Simmonds, 2002; Schmidt et al., 2005; Lee et al., 2007; Yoshimura et al., 2008; Tindall et al., 2009; Risi et al., 2010; Ishizaki et al., 2012] offer an alternate approach to providing isotope distributions. These models simulate the three-dimensional structure of water vapor isotope distributions with an explicit consideration of the complex water-phase changes associated with moist physical processes in the global atmosphere. As a result, they can provide maps

at any scale, but their temporal variability did not initially agree well with observations [Hoffmann *et al.*, 2000]. The reason for this poor isotope simulation is partly the imperfect representation of atmospheric circulation by the AGCMs, which are forced by only the observed sea surface temperature. It is also associated with the AGCM's inability to simulate the surface hydrological cycle effectively [Yoshimura *et al.*, 2006].

Yoshimura *et al.* [2003] concluded that the isotopic AGCMs would be capable of simulating day-to-day isotopic variations in precipitation more accurately if the large-scale circulation fields were simulated more accurately. Considering this, Yoshimura *et al.* [2008] performed an isotopic AGCM applying spectral nudging toward the atmospheric analysis using the NCEP/DOE Reanalysis [R2; Kanamitsu *et al.*, 2002b]. This procedure mimics the data assimilation but without any observed isotopic information. The nudging run reproduced isotope variation for a wide range of time scales, from daily to inter-annual. However, for the daily variations in isotopes in precipitation, the nudged AGCM experiment did not outperform a simple horizontally two-dimensional offline simulation in which the observed precipitation was used. This was mainly due to the poor simulation skill of the amount of precipitation in the AGCMs.

Recent advances in remote sensing observations of water vapor isotopes from satellites, particularly HDO, have increased the amount of observed data dramatically. Zakharov *et al.* [2004] retrieved latitudinal climatology for column water vapor HDO using the Interferometric Monitor for Greenhouse gases sensor (IMG) on the Advanced Earth Observing Satellite 1 (ADEOS1). Worden *et al.* [2006] retrieved low-level atmospheric water vapor HDO over the tropical regions at fine temporal and spatial resolutions using the Tropospheric Emission Spectrometer (TES) onboard the Aura spacecraft, and Payne *et al.* [2007] retrieved the global distribution of upper troposphere and stratosphere water vapor HDO on a monthly basis using the Michelson Interferometer for Passive Atmospheric Sounding (MIPAS) on Envisat. Similarly, Frankenberg *et al.* [2009] first retrieved the atmospheric column-averaged δD with the SCanning Imaging Absorption spectroMeter for Atmospheric CHartography (SCIAMACHY) on Envisat, and the method was also used for the Greenhouse gases Observing SATellite (GOSAT) [Frankenberg *et al.*, 2013]. One of the latest satellite products was reported by Lacour *et al.* [2012] with the Infrared Atmospheric Sounding Interferometer (IASI) on the Meteorological Operational satellite program (MetOp). This product provides a much larger amount of data due to its "hyper-spectral" sensor. Although limitations still exist in terms of the spatial and temporal coverage, resolution, precision, and accuracy, these maps have enabled a greater understanding of the basic distribution of isotopes and the physical processes that drive isotope distributions.

Comparisons of isotopic AGCMs and satellite products for the vapor isotope ratio were performed by Yoshimura *et al.* [2011], Risi *et al.* [2012a, 2012b], Lee *et al.* [2012], Lee *et al.* [2013], and S. J. Sutanto *et al.* (Global scale remote sensing of water isotopologues in the troposphere: Representation of first-order isotope effects, submitted to *Atmospheric Measurement Techniques*, 2014). As Yoshimura *et al.* [2011] mentioned, an overall consistency was found between the model and the satellite observations, but there were some discrepancies. Such discrepancies could be corrected by performing data assimilation, which may lead to a significant improvement in the four-dimensional analyses of the water isotope ratio distribution. Furthermore, this would in turn provide us with information that could be used to investigate atmospheric hydrological cycles further.

The main objective of this study was to evaluate the potential of water vapor isotope information in atmospheric analyses. Assimilated isotopic information would not improve the dynamic fields in a physical sense because stable water isotopes are rare, inactive, and fully dependent on atmospheric dynamic and physical processes. However, because isotopic information is a result of all the dynamic and physical processes, including it in an observation operator in data assimilation may improve the atmospheric analysis. The result would depend strongly on the relationship between the accuracy and the availability of isotopic observations and the accuracy of other atmospheric observations.

In the following section, our methodology is described. This includes specifications of the model, the data assimilation algorithm, the data assimilation system, and the experimental design. The third section presents the results. In the fourth section, we discuss the preferred characteristics of isotope observations from the perspective of data assimilation and the technical issues associated with the use of proxy data assimilation for past climates. Finally, a summary and conclusions are presented.

2. Description of Model, Data, and Data Assimilation Scheme

2.1. Isotope-Incorporated Atmospheric General Circulation Model

Gaseous forms of isotopic species (HDO and H₂¹⁸O) were incorporated into the Scripps Experimental Climate Prediction Center (ECPC) Global Spectral Model (GSM) as prognostic variables in addition to water vapor, and the model was named isotope-incorporated GSM (IsoGSM). The GSM was based on the medium-range forecast model used at NCEP to perform operational analyses and to make predictions [Kanamitsu *et al.*, 2002a]. The model's physics packages include longwave and shortwave radiation [Chou and Suarez, 1994], relaxed Arakawa–Schubert convective parameterization [Moorthi and Suarez, 1992], non-local vertical diffusion [Hong and Pan, 1998], mountain drag [Alpert *et al.*, 1988], shallow convection [Tiedtke, 1983], and the Noah land surface scheme [Ek *et al.*, 2003].

The isotopic tracers were independently advected by the dynamic processes, whereas they were treated as water vapor in the physical processes, with a small but significant isotopic fractionation associated with phase transitions. These physical processes include precipitation (convective precipitation and large-scale condensation) and surface and boundary layer processes. Note that no isotopic fractionation occurs from terrestrial evapotranspiration, i.e., 100% transpiration is assumed. The isotopic ratio of land surface storage (one snow layer and four soil layers) are also calculated in accordance with the isotopic mass balance equations, assuming that evapotranspiration and surface runoff occur only from the first layer of the soil and that base runoff occurs from the deepest (fourth) layer of the soil without fractionation.

The equilibrium fractionation factors were taken from *Majoube* [1971a, 1971b]. Most of the fractionation at a phase transition can be assumed to occur at thermodynamic equilibrium, except for three particular cases: (1) surface evaporation from open water [Merlivat and Jouzel, 1979], (2) condensation from vapor to ice in super-saturation conditions under -20°C [Jouzel and Merlivat, 1984], and (3) evaporation and isotopic exchange from liquid raindrops into unsaturated air [Stewart, 1975]. These phase changes are associated with kinetic fractionation, where the difference in molecular diffusivities plays a key role when the exchange occurs under conditions away from the thermodynamic equilibrium. For consistency with other published isotopic AGCM results, we used the isotopic diffusivity coefficients measured by Merlivat [1978]. Cappa *et al.* [2003] measured slightly different values and reported a deuterium excess that was systematically 3‰ higher, but this had a negligible impact on variability [Schmidt *et al.*, 2005]. For the equilibrium fractionation, the Rayleigh distillation theory was applied for vapor condensation during all of the precipitation processes. These sets of isotopic parameterizations are commonly used in many AGCMs, following the pioneering work of Joussaume *et al.* [1984].

The overall performance of the IsoGSM was fairly consistent with other isotopic AGCMs. To increase its accuracy, Yoshimura *et al.* [2008] ran IsoGSM with a spectral nudging technique [Yoshimura and Kanamitsu, 2008] for a global simulation from 1979 to 2006, and it has recently been extended toward 2013. An important advantage of spectral nudging is that the analysis provides more realistic isotope variation for a wider range of time scales from daily to inter-annual [e.g., Uemura *et al.*, 2008; Yoshimura *et al.*, 2010; Uemura *et al.*, 2012; Zhu *et al.*, 2012; Farlin *et al.*, 2013]. Comparisons with the limited station observations and global simulation results from other isotopic AGCM simulations revealed that the current simulation agreed better with the observations at those time scales.

2.2. Local Ensemble Transformed Kalman Filter (LETKF)

The Ensemble Kalman Filter (EnKF) ensures the feasibility of the extremely time-consuming Kalman filtering (which is considered to be the “gold standard,”) by performing computations in a subspace of perturbation runs, with the dimension of the subspace in the order of 10 to 100 (in contrast to 10^6 – 10^8 for the model). The EnKF automatically estimates and uses the background error covariance that reflects the “errors of the day” instead of the fixed error covariance used commonly in typical three-dimensional variational methods [e.g., Parrish and Derber, 1992]. Furthermore, the EnKF does not use the adjoint code of a forecast model that is required by the four-dimensional variational method (4D-Var), but its performance is equivalent to that of the 4D-Var method [Kalnay *et al.*, 2007; Miyoshi and Yamane, 2007]. Making an adjoint code for an AGCM is practically very difficult because there are many irreversible processes in the numerical codes, and the isotopic fractionation associated with moist processes makes it even more difficult. This study therefore used a type of EnKF to assimilate isotopic observations.

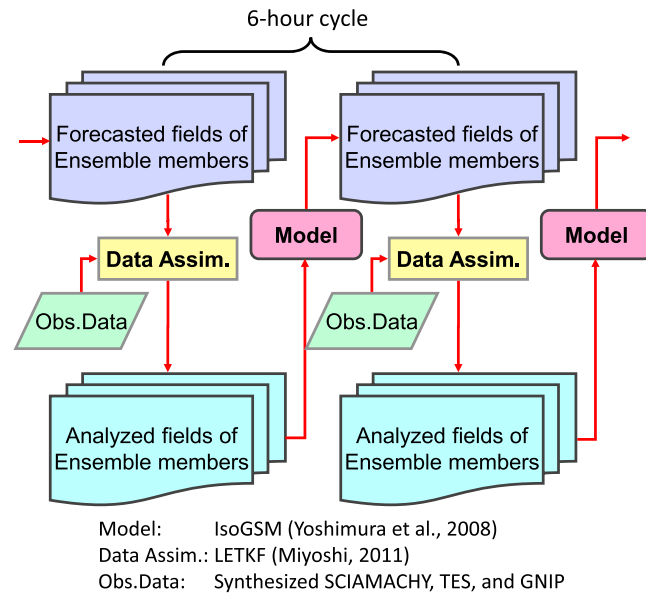


Figure 1. Schematic representation of the ensemble Kalman filter data assimilation system using Isotope-incorporated Global Spectral Model (IsoGSM) and local transform ensemble Kalman filter (LETKF).

Ott et al. [2002] introduced a square root filter, where efficiency is achieved by performing the Kalman filter analysis at each grid point based on the local (in space) structure of the ensemble forecasts within a 3D-grid point cube that includes neighboring grid points. The Kalman filter equations are solved for each grid point using the singular vectors of the ensemble as a basis within the local volume. This method, known as the Local Ensemble Kalman Filter (LEKF), allows all of the observations within the local volume to be processed simultaneously, and because the analysis at each grid point is performed independently from other grid points, it is ideal for parallel implementation. Hunt et al. [2004] and Hunt et al. [2007] extended the method to a Local Ensemble Transform Kalman Filter (LETKF) using an updated version of the Ensemble Transformed Kalman Filter

(ETKF) [Bishop et al., 2001] that is applied locally, as in Ott et al. [2004]. The localization is based on the choice of observations used for each grid point. Because the LETKF does not require any orthogonal basis, the Singular Value Decomposition (SVD) at each grid point is no longer needed, reducing the computational cost compared to the original LEKF. For a high-resolution quasi-operational Data Assimilation System (DAS), the LETKF approach has several advantages [Whitaker et al., 2008]. This study therefore used the LETKF for the assimilation of vapor isotope observation data.

2.3. Development of the Data Assimilation System

As explained previously, the data assimilation system developed in this study uses IsoGSM and LETKF. Both applications are independent, so that the core of the assimilation system acts as an interface between them. Specifically, IsoGSM outputs a forecasted snapshot of zonal and meridional wind speed, air temperature, and specific humidity, as well as mixing ratios of HDO and H₂¹⁸O in three dimensions and surface pressure in two dimensions. They are referred to as the “first guess” in the assimilation system and passed to the LETKF. The LETKF solves the mathematical equations using the first guess and observation data for the corresponding time and outputs the “analysis” in the same format as the first guess but with slightly different values. This analysis fields are given to IsoGSM as the initial condition for the next data assimilation cycle. Figure 1 shows the calculation flow of the data assimilation system.

It should be noted that in this data assimilation system, we used the δD and δ¹⁸O of water vapor instead of the mixing ratios of HDO and H₂¹⁸O, although the model directly predicts the mixing ratios. δD (and similarly δ¹⁸O) is defined as:

$$\delta D = 1 - \frac{q_{HDO} / q_{H2O}}{\left(q_{HDO} / q_{H2O} \right)_{std}},$$

where q_{HDO} is the mixing ratio of HDO in the air (in kg/kg) and q_{H2O} is the specific humidity of water vapor (also in kg/kg). The subscript “std” indicates the standard, i.e., Standard Mean Ocean Water or SMOW. To the first order, q_{HDO} and q_{H2O} vary similarly, and δD variations are of the order of a few tenths of ‰. Therefore, data assimilation of q_{HDO} would yield results similar to the assimilation of q_{H2O} itself. We wanted to obtain independent information for δD and δ¹⁸O in this study, so the system was converted from q_{HDO} to δD when the data were inputted from IsoGSM to LETKF, and reconverted from δD to q_{HDO} when the data were inputted from LETKF to IsoGSM.

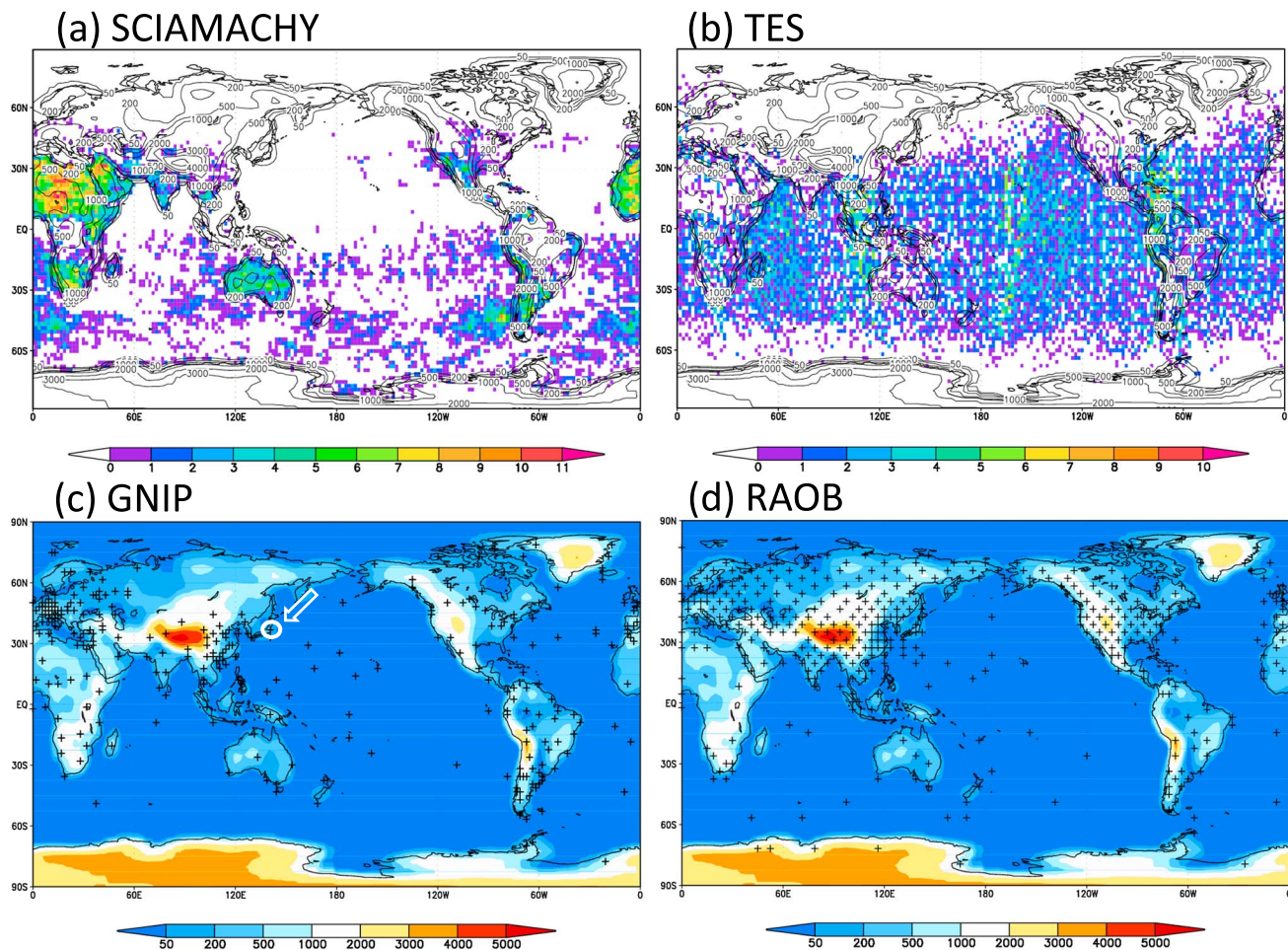


Figure 2. Spatial distributions of observation systems mocking (a) SCanning Imaging Absorption spectroMeter for Atmospheric CHartography (SCIAMACHY) measuring the vertical column water vapor isotope ratio, (b) Tropospheric Emission Spectrometer (TES) measuring the mid-tropospheric water vapor isotope ratio, (c) a virtual network of in situ surface water vapor isotope ratio on Global Network of Isotopes in Precipitation (GNIP) sites, and (d) the pseudo network of RADiosonde OBservations (RAOB). For Figures 2a and 2b, the number of measurements in a grid within January 2006 is shown by shading. For Figures 2c and 2d, site location is shown by crosses, the surface topography is shown by shading, and the circle with an arrow indicates the location of the results shown in Figures 3 to 5.

2.4. Experimental Design and Synthetic Observation Data Sets

In this study, for the first trial of data assimilation for a new physical property, we adopted the framework of the observation system simulation experiment (OSSE), as in several other studies [Kang et al., 2011, 2012]. In an OSSE, synthetic observations that would be obtained if satellite or ground-based sensors were operated are used instead of the actual observations. The synthetic observation data sets are generated from a mock “truth” data set, which in this case, was one of the ensemble members of the IsoGSM simulations for the corresponding period. To do this, we executed a free-run forced only by historical sea surface temperature (SST) and sea ice data for 2 years: 1 January 2005 to 1 January 2007. We selected a 1-month period after the first year (i.e., 1 January to 1 February 2006) from the 2-year data as the “truth” or “nature run.” It should be noted that a 1-year spin-up is enough to minimize the possibility of the model’s drift when it runs from the realistic state of the atmosphere. The model’s drift would serve as an artificial constraint, which needs to be eliminated.

Three types of isotopic observation data set were used in this study. The first was a mock of SCIAMACHY data, assuming that the atmospheric column δD was measured. Figure 2a shows the real observed data for the month of January 2006; in total ~10,000 data points per month were obtained in the horizontal resolution of IsoGSM (T62; 200×200 km grid) by averaging multiple measurements in the same grid during a 6-h period [Yoshimura et al., 2011]. The second was a mock of TES data, assuming that δD at the closest level to 600 hPa was measured. There is vertical profile of sensitivity for the instrument, and it is therefore necessary to apply the

Table 1. Specification of the Experiments^a

	Column Averaged δD	600 hPa δD	2 m δD	2 m $\delta^{18}O$	Wind Speed, Temperature, Humidity and Surface Pressure
No Observation (NoObs)					
SCanning Imaging Absorption spectroMeter for atmospheric chartography (SCIA)	X				
Tropospheric Emission Spectrometer (TES)		X			
Global Network of Isotopes in Precipitation (GNIP)			X	X	
All of SCIA, TES, and GNIP (ALL)	X	X	X	X	
RAdiosonde OBServations (RAOB)					X
RAdiosonde OBServations and all of SCIA, TES and GNIP (RAOBALL)	X	X	X	X	X

^a“X” indicates the variable inputted in each experiment.

averaging kernels (AK) of the satellite instrument’s retrieval algorithms to the modeled fields to correctly compare the TES and model [e.g., *Yoshimura et al.*, 2011]. Thus, although it is assumed that TES measurement is at a specific level (about 600 hPa) in our current ideal experiments, it has a vertically broader representation in reality. This issue will be revisited in the section addressing the analysis increment (Section 3d). We used a realistic spatial and temporal distribution in the similar manner as SCIAMACHY data. In total, ~15,000 data points were recorded as valid measurements in the IsoGSM resolution (Figure 2b). The third was a mock of the in situ network of surface air water vapor δD and $\delta^{18}O$ measurements. Currently, such an observation network does not exist, but we assumed a situation where major laser vapor isotope instruments (e.g., Picarro and Los Gatos Research (LGR)) were installed in the currently active GNIP (Global Network of Isotope in Precipitation) [International Atomic Energy Agency, 2001] sites (~200 sites worldwide; see Figure 2c). Considering recent technical and manufacturing improvements and international efforts to disseminate these instruments to many countries (such as the IAEA program), we assume that such a vapor isotope observation network is realistic. We assumed that 6-hourly measurements for both water vapor δD and $\delta^{18}O$ at 2 m were available at ~200 sites. Again, only one site in each grid box was used for data assimilation. Finally, we make a virtual radiosonde network over the world with ~400 sites (Figure 2d). At each site, we assume that there is 6-hourly measurement of surface pressure and vertical profiles for wind speed, temperature, and humidity.

When the synthetic observation data were generated from the “true” atmospheric data, a random error was incorporated. For the SCIAMACHY, TES, and GNIP data sets used in this study, we assumed standard deviations of 100‰ and 10‰ for δD and $\delta^{18}O$, respectively. These values are high, especially for the in situ laser spectrometric instruments. However, in practice, there is an issue of the spatial and temporal representation of the observation data. Therefore, it is common to increase the observation error to ensure that the analysis functions appropriately. The random observation errors for wind speed, temperature, humidity, and surface pressure from radiosonde measurements were 1 m/s, 1 K, 1 g/kg, and 1 hPa, respectively.

Using these synthetic observation data sets, we performed four experiments, as shown in Table 1. Additionally, a No Observation (NoObs) experiment was performed without using any observation data. The NoObs experiment was used as a reference by providing the maximum forecasting error. SCIA, TES, and GNIP experiments individually used the synthetic SCIAMACHY, TES, and GNIP data sets, respectively. Finally, an ALL experiment used all the data sets simultaneously. All experiments were for the same period (1 January to 1 February 2006) and used the same ensemble size (20), same model resolution (horizontally T62 and vertically 28 sigma levels), same dynamics and physics package, same boundary data (NCEP SST and sea ice distribution), and same localization (10 regions). We intend to undertake further experiments at different times of the year, particularly the summer months in the northern hemisphere. Furthermore, the adaptive covariance inflation [Miyoshi, 2011] was activated. The initial conditions of each ensemble member were taken from the “truth” data for different dates in January 2006. The atmospheric states at 0000 UTC on 2, 3, 4... and 21 January were used as the initial conditions of the 20 different members at 0000 UTC 1 January. Despite the fact that the initial condition of some of the members was similar to the “truth” (particularly the condition from 2 January), there is no problem in our experiment because the results were compared with the NoObs experiment, which used an identical set of initial conditions to the other experiments.

In addition to these experiments, we undertook two more experiments, one with a more conventional meteorological measurement network of operational radiosonde instruments for wind speed, temperature,

humidity, and pressure RADiosonde OBServations (RAOB), and the other with the radiosonde network and isotopic observation data sets described above RADiosonde OBServations and all SCIA, TES, and GNIP (RAOBALL). All other configurations were identical to the earlier experiments. These experiments have a different purpose from the others, i.e., to quantify the impact of observations when the atmospheric state is already well constrained. The results of these additional experiments are presented in the Discussion section.

3. Results

3.1. Temporal Variations at a Specific Grid Point

First, we focused on temporal variations of multiple variables at a single site. We arbitrarily chose a grid including Tokyo (140°E and 35°N; indicated in Figure 2c) because this area contains a relatively dense network of GNIP observation sites, and TES and SCIAMACHY data are available for locations nearby. Figure 3 shows 6-hourly temporal variations for $\delta^{18}\text{O}$ of water vapor at the lowest model level (about 50 m above the surface). As Figure 3a indicates, the “truth” (black line) and each ensemble member (gray lines) were not coherent. The ensemble members diverged independently of each other, so the ensemble mean (green line), i.e., analysis, did not match the “truth.” This situation is similar to the SCIA (Figure 3b) and TES experiments (Figure 3c) with a slight reduction in ensemble spread. This is likely due to the scarceness of the data in SCIAMACHY and TES, as shown in Figures 2a and 2b. Neither covers the west of Japan, which is likely to be the upstream region for the site. However, in the GNIP experiment (Figure 3d), the analysis was much closer to the “truth,” reproducing the synoptic scale (4–5 days scale) variations well with a much smaller ensemble spread, particularly for 11 to 16 and 21 to 26 January. This is because there were observation sites not only in Tokyo but also over the upstream region (i.e., the Chinese subcontinent and Korean peninsula). A similar result was found in the ALL experiment (Figure 3e), indicating that GNIP data were the most effective for improving the accuracy of the analysis of the temporal variation of surface water vapor $\delta^{18}\text{O}$ at this site.

The results for δD were similar to those for $\delta^{18}\text{O}$ (data not shown). This indicates that due to the well-known linear relationship between $\delta^{18}\text{O}$ and δD (i.e., $\delta\text{D} = 8 \times \delta^{18}\text{O} + 10$), there was essentially no difference in observations constrained by $\delta^{18}\text{O}$ or δD . D-excess, as determined by the departure from the linear relationship (i.e., $\text{D-excess} = \delta\text{D} - 8 \times \delta^{18}\text{O}$), cannot be constrained in this framework. This is reasonable because we used relatively large random observation errors (100‰ and 10‰ for δD and $\delta^{18}\text{O}$, respectively), and therefore the random error range of D-excess was also large (more than 100‰) relative to the model error range, which is smaller than that of δD and $\delta^{18}\text{O}$ due to the strong coherency between the two.

The above evaluation was used for the isotopic ratios, which were then input to the system. Thus, the results confirmed that the assimilation system worked as intended. The main objective of the study was to determine whether isotopic constraints would generate an improvement in the other atmospheric fields. Figure 4 shows a similar evaluation to that shown in Figure 3, but for air temperature. As with the $\delta^{18}\text{O}$ variations, there was no analysis skill in NoObs (Figure 4a), and very little in the SCIA and TES experiments (Figures 4b and 4c). However, in the GNIP experiment, there was an obvious improvement, with the warmer periods of 11–13 and 28–29 January being simulated well with a smaller ensemble spread (see Figure 4d). No additional improvement in the ALL experiment was apparent, although the temperature shift from 26 to 28 January was closer to the truth than in the GNIP experiment (see Figure 4e). The fact that the isotopic constraint improved the temperature analysis could be explained by the correlation between the isotopic ratio and air temperature due to the thermodynamic process, i.e., Rayleigh distillation. Due to Rayleigh distillation, there was a poleward gradient of vapor isotopic ratio, which was closely correlated to the temperature and humidity gradients. Thus, when a dynamic process operated to lower the air temperature, such as the northerly wind in Tokyo, it would be associated with lower humidity and a lower isotopic ratio. This is a rather weak tendency, and it is obviously not always valid in the Earth system on a 6-hourly time scale (there might be a case with a similar northerly wind, which increases the isotopic ratio), but the data assimilation system would have taken this relationship into account and obtained a better solution to minimize the thermodynamic inconsistency.

Figure 5 shows the zonal wind speed variations in the same grid. In general, a similar observation could be made with a better analysis skill in the GNIP (Figure 5d) than in the NoObs experiment (Figure 5a). However, the improvement was not as obvious as for the air temperature or isotopic ratio. This is because the isotopic ratio has an even weaker relationship with wind speed than with air temperature. Qualitatively speaking, a westerly wind may result in a smaller isotopic ratio because a larger amount of precipitation occurs from the

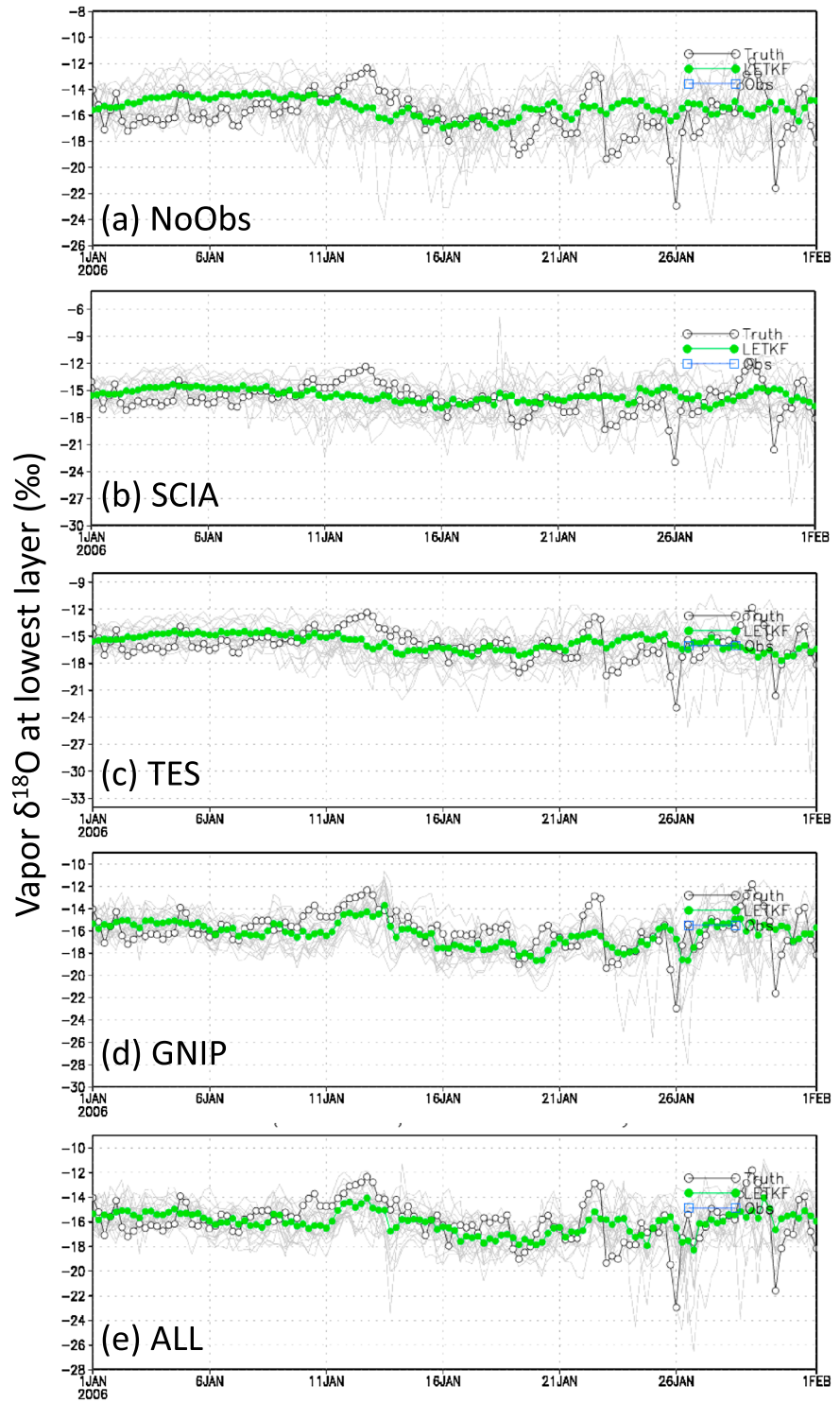


Figure 3. Temporal variations of the water vapor $\delta^{18}\text{O}$ at the lowest model level in a grid including Tokyo (140E/35N) for (a) NoObs, (b) SCIA, (c) TES, (d) GNIP, and (e) ALL experiments. Black lines indicate “truth,” each of the gray lines indicates an ensemble member, and green lines indicate the ensemble member or “analysis” from the data assimilation system.

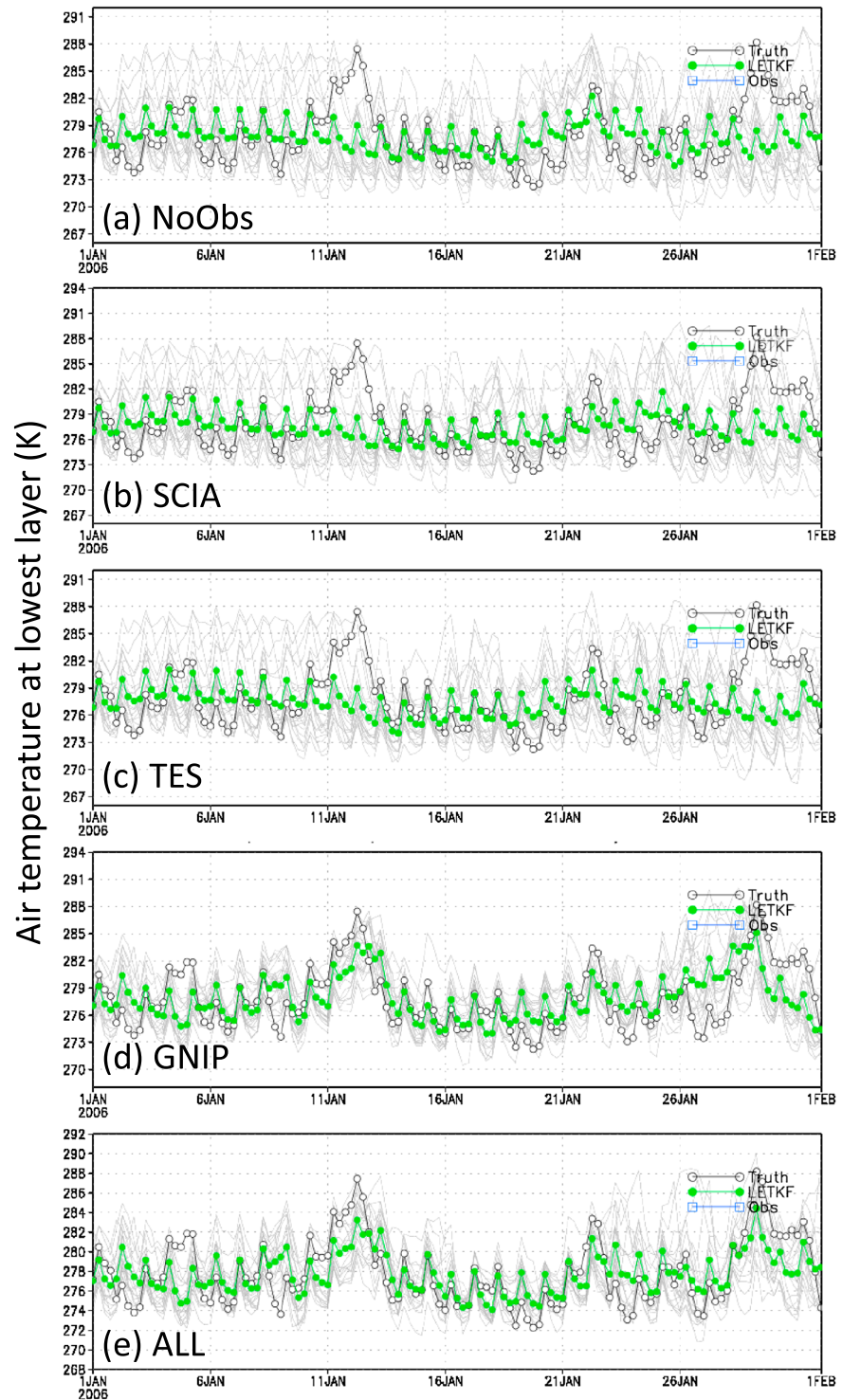


Figure 4. Similar to Figure 3, but for air temperature at the lowest model level.

air mass than would occur from an equivalent air mass from the east. What the data assimilation system calculates is apparently more comprehensive than such a simple relationship.

The above analyses were undertaken for a specific site in East Asia and were largely qualitative, although an improvement in the isotope data assimilation was clear. In the next section, we describe a more quantitative evaluation and analyze the impact of geographical characteristics on the data assimilation.

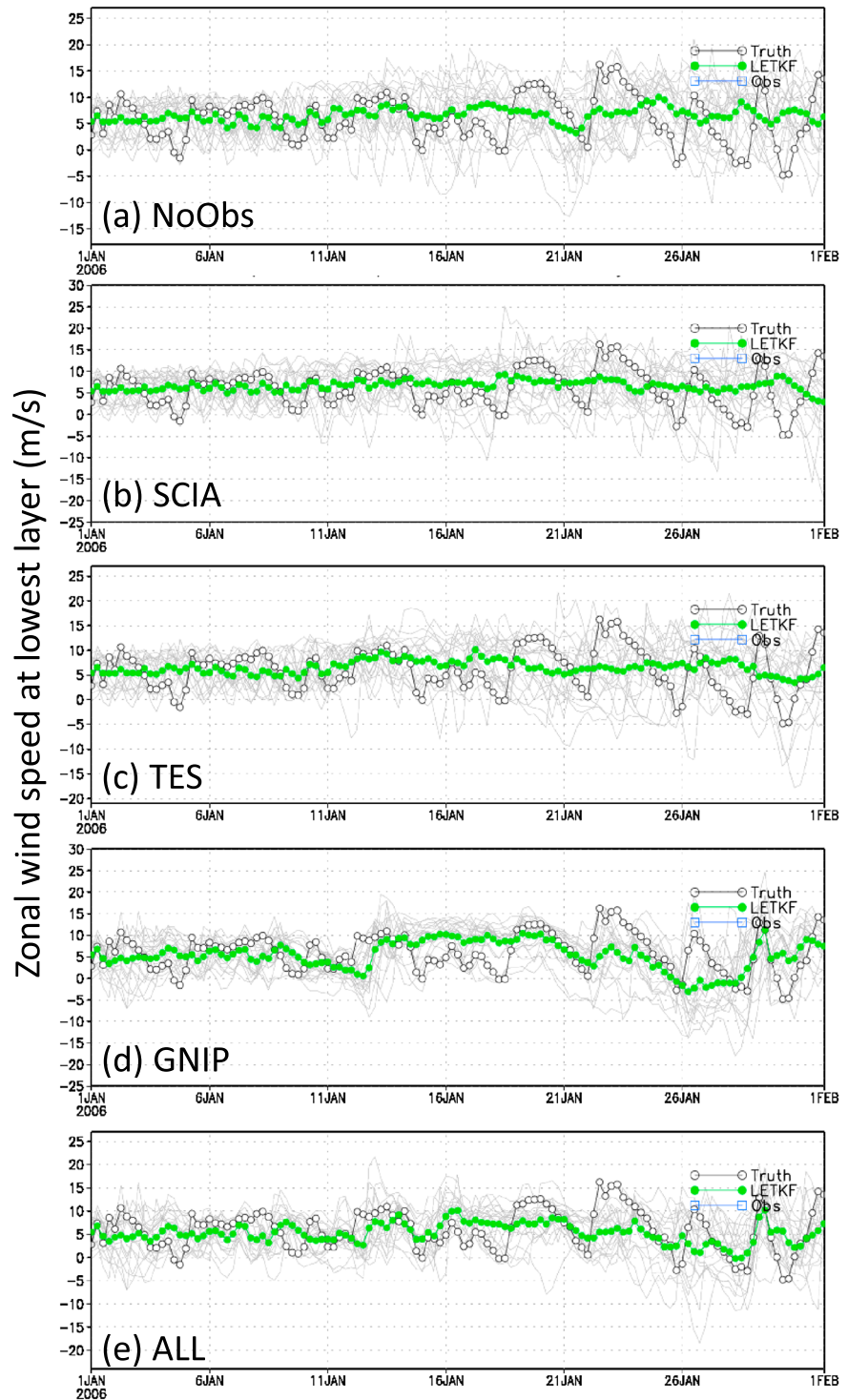


Figure 5. Similar to Figure 3, but for zonal wind speed at the lowest model level.

3.2. Global Evaluation of the 6-Hourly RMSD

Figures 6 to 8 show the global distribution of the 1-month averaged 6-hourly root-mean-square difference (RMSD) between the analysis (ensemble mean) and the “truth” for the NoObs experiment (panel “a”) and the reduction in the RMSD in the other experiments (panels “b” to “e”). Note that the positive number in RMSD

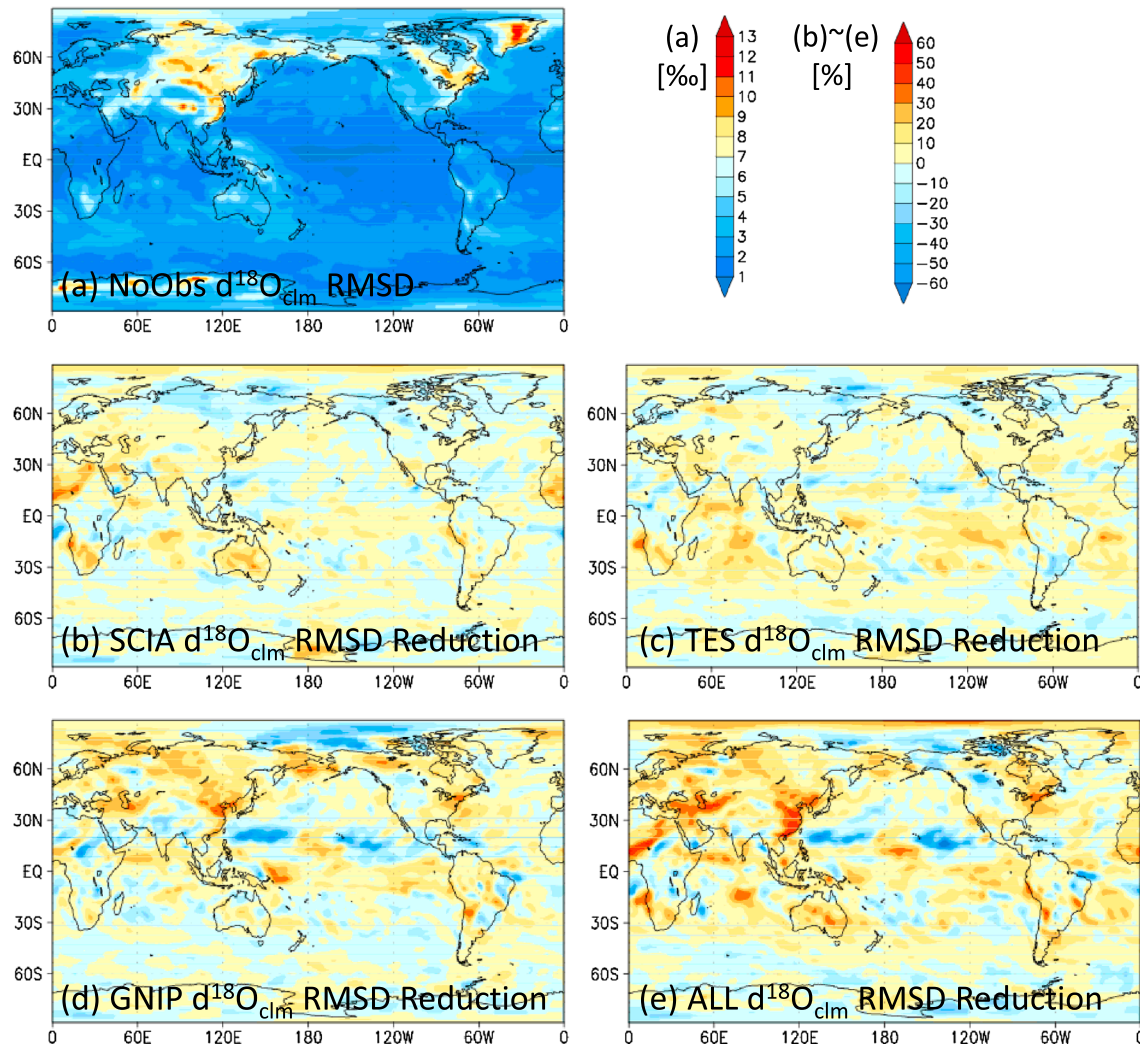


Figure 6. (a) Oxygen isotope ratio ($\delta^{18}\text{O}_{\text{clm}}$) in the NoObs experiment using 1-month averaged, 6-hourly root-mean-square difference (RMSD) in the atmospheric column. Figures 6b, 6c, 6d, and 6e are the reductions in RMSD compared to (a) as percentages for the SCIA, TES, GNIP, and ALL experiments, respectively.

reduction (hot colors in the figures) shows an improvement compared with the NoObs experiment in terms of the short-term variability of the designated variable.

The results for atmospheric column $\delta^{18}\text{O}$ ($\delta^{18}\text{O}_{\text{clm}}$) are shown in Figure 6. The RMSD in NoObs shows larger values in the high latitudes over land because of the larger short-term variability in $\delta^{18}\text{O}_{\text{clm}}$, which is mainly associated with air temperature variability. In the previous section, any improvement in the analysis of the SCIA and TES experiments was not as obvious as in the GNIP experiment, but as can be seen in Figures 6b and 6c, there were reductions (20–35%) in RMSD over locations such as the Sahel and Australian deserts in SCIA (Figure 6b) and the Indian Ocean and tropical regions of Pacific Ocean and Atlantic Ocean in TES (Figure 6c). This is consistent with the distribution of observation data shown in Figures 2a and 2b, respectively.

Figure 6d indicates that the improvement in analysis skill was greater in the GNIP experiment than SCIA or TES. In some areas such as northern China, Turkey to Central Asia, and the northeast coast of United States, the reduction in the RMSD reached 30–40%. This reduction corresponds to those areas that have observation sites located in their upstream regions (see Figure 2c). The greatest improvement was recorded in the ALL experiment (Figure 6e). The distribution of the apparently improved area was similar to that of the GNIP experiment, but the reduction in RMSD was 40–50% in locations such as east China and Central Asia. This indicates that the additional information from SCIAMACHY and TES has a significantly positive impact.

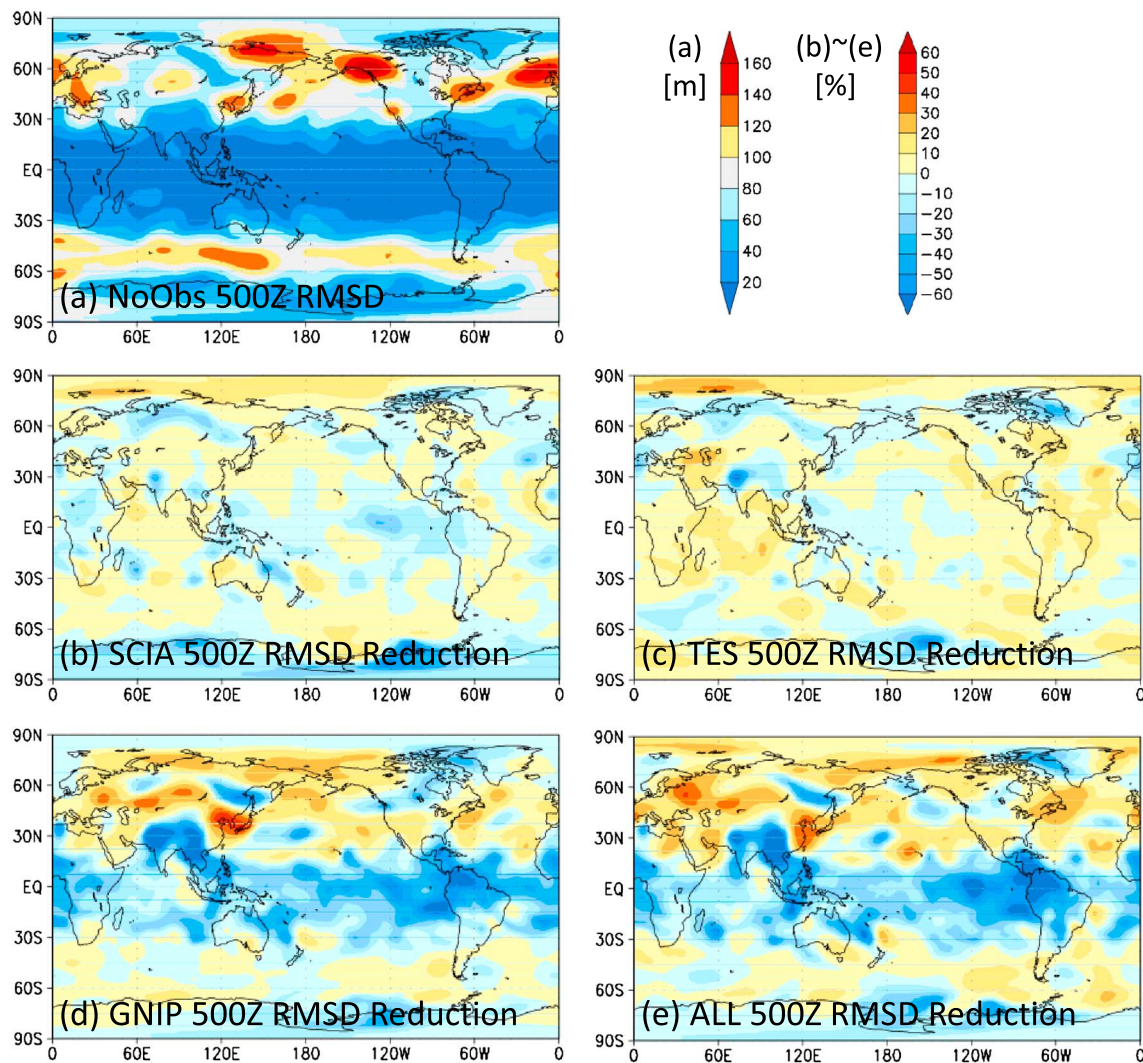


Figure 7. Similar to Figure 6, but for geopotential height at 500 hPa.

It should be noted that the impact of isotope data assimilation was not always positive, and there was an obvious deterioration in all four experiments, particularly where little observation data was inputted. The areas affected include Eastern Siberia in the SCIA and TES experiments and the tropical Pacific Ocean and Arctic Ocean in the GNIP and ALL experiments.

The RMSD of 500 hPa geopotential height (500Z) is a good indicator of the analysis and forecast skill for the synoptic weather pattern in the mid- to high latitudes. In Figure 7a, an RMSD of 500Z in the NoObs experiment is shown. Without any atmospheric constraint, the 500Z RMSD extends for more than 150 m in some regions due to the inherent chaotic behavior of the atmosphere, and this is particularly associated with the westerly jets in both hemispheres. The improvement in the SCIA experiment was not large (10–15% reduction in RMSD) for some locations, e.g., western Australia (Figure 7b). The TES experiment showed a slightly greater improvement (20–30% reduction) for locations in Turkey to Central Asia area and over the Indian Ocean. The GNIP experiment produced different results with a large improvement in the area from Korea to Japan (45% reduction), and some other mid-latitude locations (20–25% reduction). The ALL experiment produced a small worldwide improvement compared to the GNIP experiment, but the latter produced a better result for the Korea to Japan area.

However, in the 500Z field, there were apparent deteriorations over the tropics, particularly in the GNIP and ALL experiments. Because the RMSD of 500Z over the tropics were smaller than those over the mid- and high

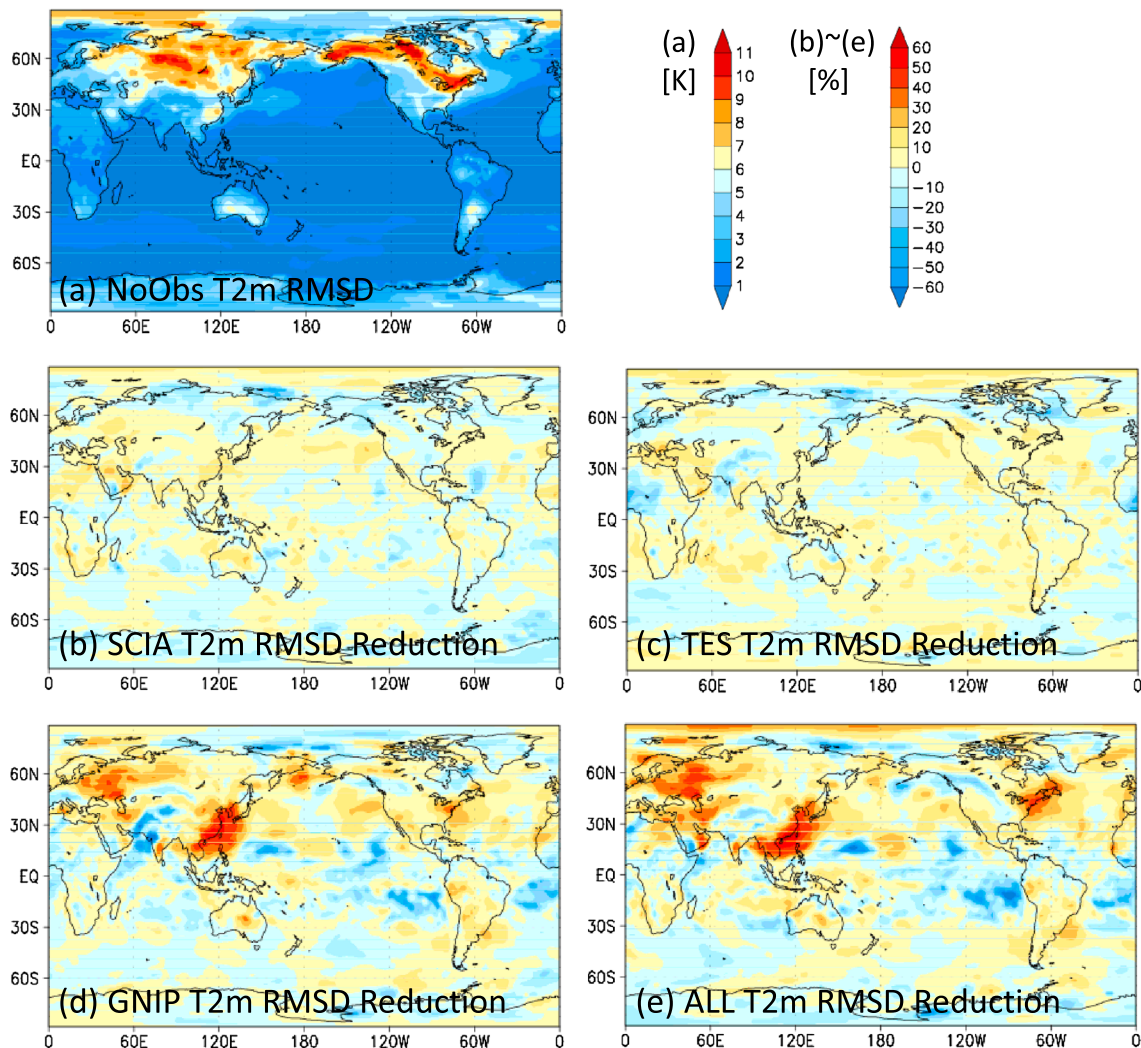


Figure 8. Similar to Figure 6, but for 2 m air temperature.

latitudes, the globally averaged RMSDs were smaller than those of NoObs. This deterioration may reflect the dynamic characteristics over the tropical atmosphere, i.e., the absence of geostrophic wind. In those areas, 500Z is controlled by local phenomena such as deep convection. The vapor isotope does not hold such information. Moreover, the more positive and stronger constraint for the mid- to high latitudes created a systematic bias over the tropics. In the SCIA and TES experiments, the dynamic constraint was weaker than that in the GNIP and ALL experiments, so that the degree of both improvement and deterioration was also smaller.

Figure 8 shows data similar to Figures 6 and 7, but for air temperature at a height of 2 m. The 1-month averaged, 6-hourly RMSD of the NoObs experiment was larger over the northeastern Eurasian continent and northern North American continent because of the large day-to-day temperature differences over high latitudes. It is worthwhile to note that because the SST and sea ice distribution were given, the surface air temperature over the ocean was strongly constrained even in the NoObs experiment. The RMSD reduction was at most 20% in both the SCIA and TES experiments. The SCIA experiment displayed an articular improvement in the Sahara Desert, Arabian Peninsula, and Australia, due to the large number of measurements over those desert areas (see Figure 2a). Although most of the TES observations were over oceans, the improvement in the RMSD over ocean was not as apparent because the RMSD in NoObs was already small in these locations.

The improvement in 2 m air temperature was much greater in the GNIP experiment than in the SCIA and TES experiments (Figure 8d). This was particularly apparent in east Europe and west Russia, Turkey, and Syria, East

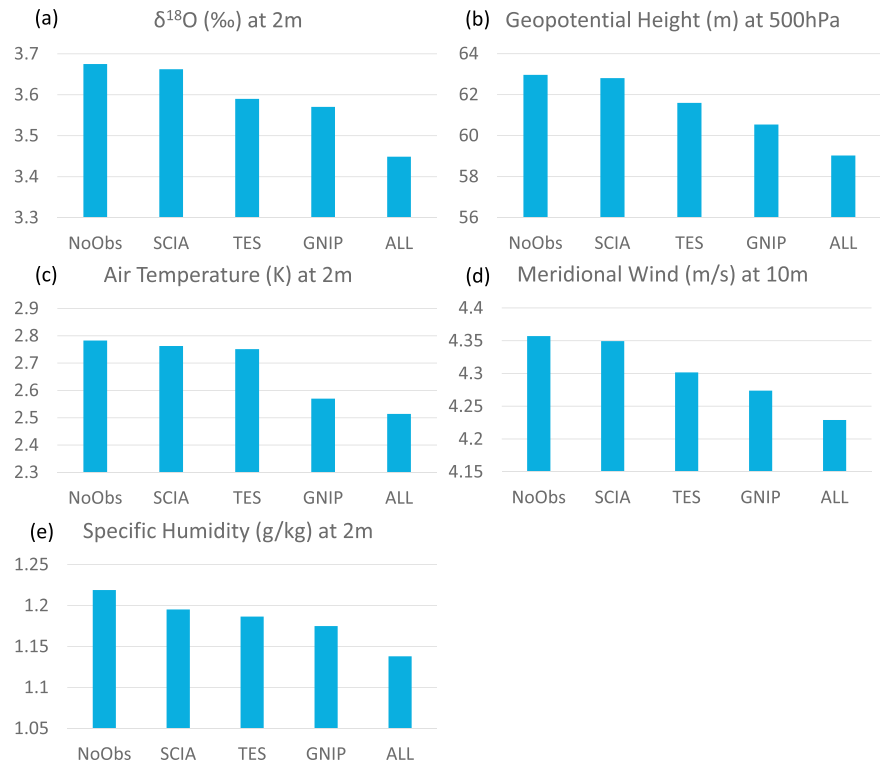


Figure 9. Global mean of 1-month averaged, 6-hourly RMSD in all five experiments for (a) 2 m $\delta^{18}\text{O}$, (b) geopotential height at 500 hPa, (c) 2 m air temperature, (d) 10 m meridional wind speed, and (e) 2 m specific humidity.

coast US (up to 40% reduction). The most remarkable improvement was in the East and Southeast Asia region and is centered on east coast China, with a >50% reduction. Because we assumed a denser in situ observation network in China, a remarkable improvement was achieved. Even though the network in Europe was denser, the improvement was not as marked as in East Asia, because the RMSD was not as large in the NoObs experiment due to the stronger SST constraint over Europe.

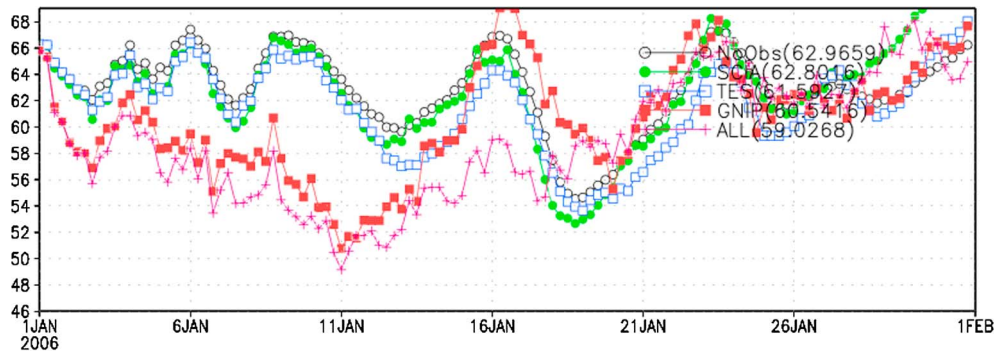
As shown in Figure 8e, the improvement achieved using all of the observation data sets in the ALL experiment was similar to the GNIP. There were slight improvements in the GNIP over the Middle East and Central Asia and East coast US (up to 45% reduction). These improvements are probably attributable to the additional information from SCIAMACHY, which has higher instrumental sensitivity in the lower part of the atmosphere.

It should be noted that there was no significant improvement in the global average of monthly averaged values in any experiment (i.e., no improvement in the bias of the model). This can be considered reasonable given the design of our experiments. With the “perfect model” assumption, i.e., only randomly distributed observation error and 6-hourly intervals of the data assimilation cycle, we intentionally configured our methodology to improve the short-term variability, i.e., diurnal to synoptic (4–5 days) scale phenomena. There were some areas where the monthly mean values were closer to the truth, but it was just a secondary effect due to the improvement in the short-term variability. In fact, there were areas with deterioration in the bias (monthly average) but improvement in the short-term variability (6-hourly RMSD).

3.3. Globally Averaged 6-Hourly RMSD

Figure 9 shows the monthly average global mean 6-hourly RMSD for all experiments for 2 m water vapor $\delta^{18}\text{O}$, 500 hPa geopotential height, 2 m air temperature, 10 m meridional wind speed, and 2 m humidity. As observed from the global distribution maps, the RMSD was generally at a maximum in the NoObs experiment and decreased in the order of SCIA, TES, GNIP, and ALL experiments. The difference in the RMSD reduction in the ALL experiment compared to NoObs was 0.2‰ in 2 m vapor $\delta^{18}\text{O}$ (Figure 9a), 3 m in 500Z (Figure 9b), 0.25 K in 2 m air temperature (Figure 9c), 0.1 m/s in 10 m meridional wind speed (Figure 9d), and 0.05 g/kg in

(a) Global RMSD in Geopotential Height at 500 hPa (m)



(b) Global RMSD in 2m Air Temperature (K)

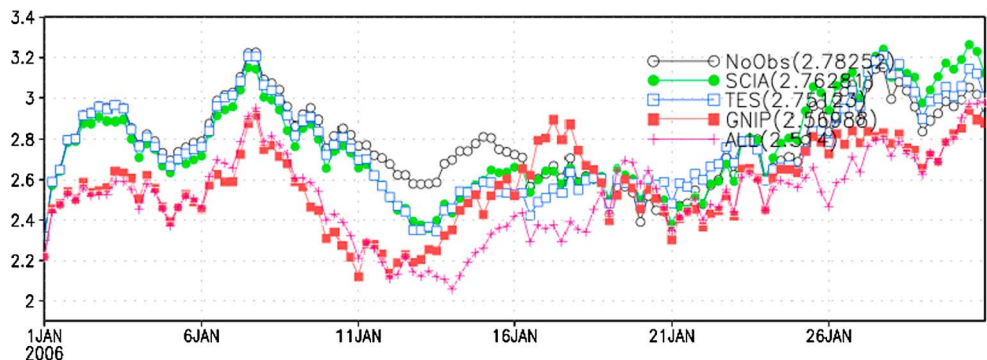


Figure 10. Temporal variations in global mean 6-hourly RMSD against the “truth” in January 2006 for (a) for geopotential height at the 500 hPa level, and (b) for 2 m air temperature. Black, green, blue, red, and purple lines show the NoObs, SCIA, TES, GNIP, and ALL experiments, respectively.

2 m specific humidity. For practical purposes, these numbers are not large but with such a limited number of measurements over the globe, finding dynamic constraints was surprising. Furthermore, Figure 9 indicates that larger number of observations (SCIA: ~10,000, TES: ~15,000, GNIP: ~48,000 data points) would further improve the atmospheric analysis skill.

Figure 10 shows the temporal variation in global mean RMSD for 500Z and 2 m air temperature. For 500Z (Figure 10a), the improvement in the GNIP and ALL experiments was apparent in the first half of the month, but not in the second half of the month. The constraint on atmospheric dynamics by using isotopic information over limited regions is weak. Therefore, the impact on the analysis skill depends on the atmospheric conditions. When the synoptic change is rapid, the dynamic fields cannot be corrected using isotopic data only. In this situation, the RMSD became similar to that of the NoObs experiment. This implies that if the atmospheric dynamic fields are constrained to some extent by direct measurements, water vapor isotopes could yield a positive impact. Thus, the impact of observations by isotopes is not always linear but depends on other observation data. This is an interesting topic that will be addressed in a future study. However, there might be some influence of the ensemble member number and the covariance inflation factor. A range of ensemble members, i.e., ensemble spread, is crucial for successful ensemble data assimilation, but currently, there is no consistent physical basis to determine the size of an ensemble member and the degree of inflation factor. This issue is beyond the scope of this study but would be worthwhile to investigate in the future.

Figure 10b shows that for 2 m air temperature the improvement by the ALL experiment was consistent throughout the period. Similar to 500Z, the improvement declined in the second half of the period but recovered at the end of the period, after 26 January. The improvement in the SCIA and TES experiments was limited, but there were some significant improvements for the period of 11 to 16 January. During the same period, the impact of the additional observations in the ALL experiment compared to GNIP was apparent.

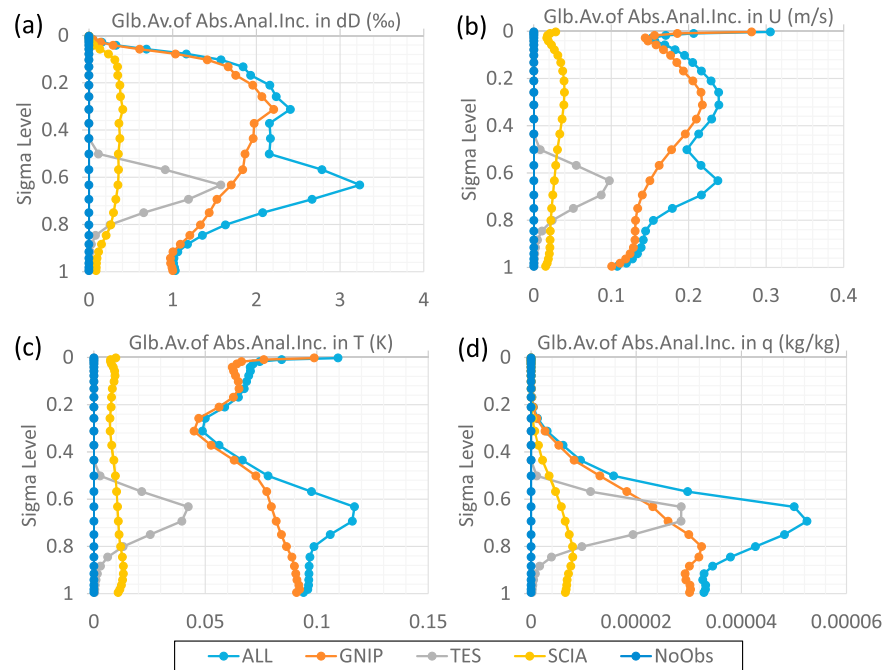


Figure 11. Vertical profiles of the global mean monthly average of absolute analysis increment for (a) vapor δD , (b) zonal wind speed, (c) air temperature, and (d) specific humidity.

3.4. Vertical Profiles of Analysis Increment and Ensemble Spread

The analysis increment is the difference between the first guess field and the analysis field, i.e., the corrections made by assimilating observations. It should be noted that the analysis increment does not necessarily improve the dynamic fields. Figure 11 shows the monthly mean global average of the absolute analysis increment in all 28 sigma levels in the model for four variables (δD , zonal wind speed, air temperature, and specific humidity).

Figure 11a shows the absolute increment for δD . There was obviously no impact in the NoObs experiment. For the SCIA experiment the impact was fairly constant at all levels (maximum 0.5‰), with the exception of the top and bottom levels. Because two-dimensional atmospheric column values were outputted in addition to the three-dimensional variables from the model, and given that the assimilation algorithm did not consider vertical localization, there was little vertical difference in the analysis increment for the SCIA experiment. However, in the TES experiment (gray line in Figure 11a) a considerable impact at the 0.8–0.5 sigma levels can be seen. This is because for the TES observation, we assumed that the highest sensitivity would be ~ 600 hPa in the three-dimensional data, and the data assimilation algorithm applied vertical localization. This vertical concentration of the analysis increment would be more disseminated when more realistic vertical representativity of TES is taken into account by using the averaging kernel.

The analysis increment for the GNIP experiment was also quite monotonous, except for the surface and top of the atmosphere. As with the atmospheric column variables, the 2 m vapor isotope ratio is outputted separately from the model, so that the data assimilation system did not take vertical localization into account. The degree of the absolute increment was larger than that of the SCIA experiment, due to the larger amount of data. In the ALL experiment, the degree of increments was similar to the linear summation of those from SCIA, TES, and GNIP, with a large increment peak at the 0.8–0.5 sigma level corresponding to the TES data set.

The basic features of the other variables (i.e., zonal wind speed (Figure 11b), air temperature (Figure 11c), and specific humidity (Figure 11d)) were similar to that of water vapor δD : a small but vertically constant increment in SCIA, an apparent mid-troposphere focus in TES, and a vertically constant large increment in GNIP, with a combination of all three in ALL. There was an exception for the zonal wind speed, for which the highest absolute increment at the top of the atmosphere corresponded to a greater wind speed at higher

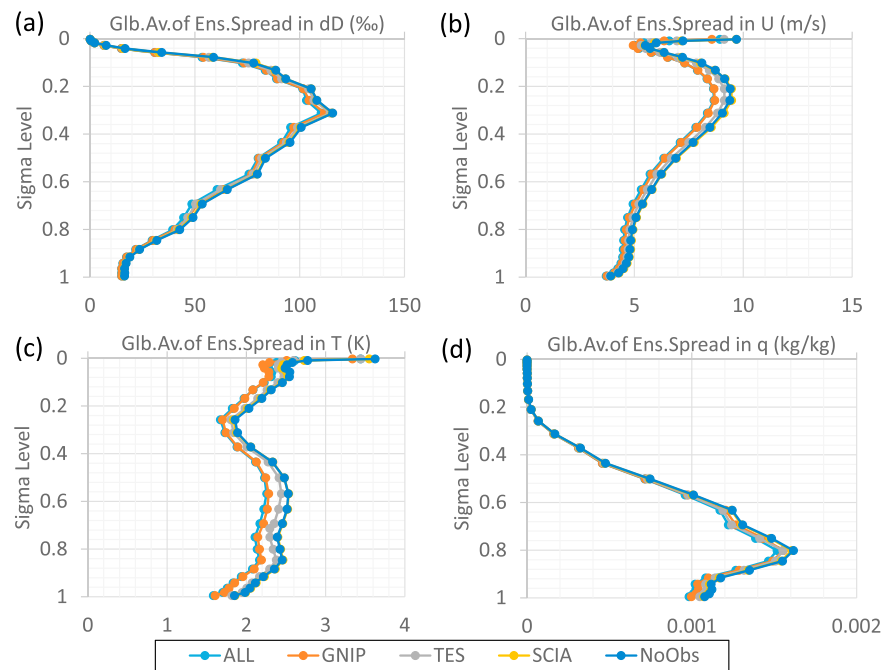


Figure 12. Similar to Figure 11, but for ensemble spread.

levels. In contrast, there was almost no increment for specific humidity at the higher levels because only a very small amount of vapor existed at the top level.

Figure 12 shows the vertical profiles of the ensemble spread in the four variables selected in Figure 11 (i.e., δD , zonal wind speed, air temperature, and specific humidity). As described above, the ensemble spread is assumed to represent the state estimation error; therefore, a larger spread represents more uncertainty in the analysis. Figure 12a shows that the largest ensemble spread was observed in the NoObs experiment. It can be seen that the data assimilation functions well as designed. However, the degree of shrinkage of the spread was not as obvious as in the global mean in δD (Figure 12a). The shrinkage of the spread was more apparent for the zonal wind speed (Figure 12b), and even more so for air temperature (Figure 12c). In general, the ALL experiments produced the lowest ensemble spread in all levels and for all variables, but the spread was almost identical to that in the GNIP experiment. This indicates that additional constraints from the TES and SCIA data sets were not sufficiently strong to reduce the ensemble spread, even though they had a significant impact on the analysis increment (Figure 11) and the RMSD (Figure 9).

4. Discussion and Future Works

4.1. Observation Impact by Isotopes in Addition to Conventional Meteorological Data

Other than those for vapor isotopes, our OSSE did not use any of the other currently available observation data sets. We thus tested two additional OSSEs with a synthetic radiosonde network (about 400 sites worldwide; see Figure 2d) for surface pressure and vertical profiles of temperature, wind speed, and humidity in 6-hourly intervals (RAOB experiment), and for all the synthetic isotopic data sets that we created (RAOBALL experiment). Table 2 is similar to Figure 9, but shows the RMSD for all prognostic variables, i.e., zonal and meridional wind speed, temperature, humidity, $\delta^{18}O$, and δD at the bottom model layer (sigma level of 0.995) and the sixth layer (sigma level of 0.8835). For both experiments, the values of RMSD were much lower than for the experiments without the radiosonde network data. This indicates that the direct measurements of wind speed, temperature, and humidity work very effectively to constrain atmospheric general circulation.

More focus should be given to the difference between RAOB and RAOBALL, i.e., the impact of observations on the vapor isotope measurements in addition to the more realistically available observation data sets. The impact of analysis using isotopic data in addition to the radiosonde network was actually small but

Table 2. Global Monthly Averages of 6-Hourly Root-Mean-Square Difference (RMSD) for All Prognostic Variables at the First and Sixth Model Layers From the Bottom

First Layer ($\sigma = 0.995$)	Zonal Wind (m/s)	Meridional Wind (m/s)	Temperature (K)	Humidity (g/kg)	Surface Pressure (hPa)	$\delta^{18}\text{O}$ (‰)	δD (‰)
RAOB	1.30	1.30	0.42	0.42	1.02	0.98	7.24
RAOBALL	1.25	1.26	0.41	0.41	0.98	0.95	7.04
Sixth layer ($\sigma = 0.8835$)							
RAOB	1.46	1.40	0.55	0.69	N/A	1.41	10.75
RAOBALL	1.40	1.35	0.54	0.67	N/A	1.37	10.41

positive for all listed variables. This limited impact indicates that because the measurements by radiosonde observation were more direct and abundant (6-hourly and at all vertical levels at ~400 sites), the analysis skill was already good, with little room for further improvement using additional vapor isotope data. However, the positive impact indicates that the additional vapor isotope ratio information, which was not previously operationally used, constrained the atmospheric field to a larger extent. This implies that in the future, when vapor isotopic fields can be measured more easily and frequently, these isotopic measurements could play a role in improving the analysis and forecast skill because they provide unique information relevant to atmospheric circulation.

4.2. Recommended Characteristics of Isotopic Observations for Data Assimilation

In this study, it was clearly shown that vapor isotope data retrieved by satellite sensors or in situ monitoring networks have the potential to constrain the atmospheric fields. However, the experiments were in an OSSE framework, which expects the most optimistic estimate of the impact of an observation by assuming a “perfect” model. Therefore, it is necessary to conduct a set of experiments using the real observation data sets.

One purpose of the OSSE was to evaluate the distribution of the data set in space and time and the measurement accuracy for analysis skill. This study revealed that a larger number of data points produced a more positive impact. The spatial distribution of the data was not tested systematically, but because the improvement was greater over the northern Pacific Ocean, which contains few GNIP stations, than over Western Europe, which has a dense network of sites (see Figures 2c and 8d), an equally distributed network is preferable for the same number of sites.

For measurement accuracy, because the optimum analysis skill was obtained when the model and observation errors were roughly identical, the observation error values of 10‰ and 100‰ for $\delta^{18}\text{O}$ and δD , respectively, worked well. When the errors were reduced into realistic values for a typical in situ laser spectrometer (1‰ and 10‰ for $\delta^{18}\text{O}$ and δD , respectively) the analysis skill deteriorated (figure not shown). Because of the small observation error, all ensemble members were more converged into the observation value, and the guess fields did not have a sufficient ensemble spread to include the consequent observation value. This issue of the observation errors needs to be investigated further but should be considered together with the issue of ensemble size and the inflation factor, because the ensemble spread is essentially the same as the model error in the ensemble Kalman Filter. Furthermore, it should be noted that the observation error characteristic is not constant in the satellite instruments, particularly in TES. The impact of variable error characteristics in time and space may be interesting to determine in a future study.

4.3. Toward Proxy Data Assimilation

By demonstrating the potential to constrain atmospheric dynamic fields by vapor isotopic information, a further challenging scientific question emerges: “Can we analyze the past climate using the available isotopic proxy information with data assimilation?” We have used isotopic information intensively to reconstruct past climates, but this approach is dependent on the empirical relationship between the isotope and the climate. The essential weakness of such a reconstruction methodology is that the relationship may vary over time. In addition, the proxy relationship is often over-simplified, with secondary or further influencing parameter(s) being ignored. Data assimilation using proxy data can potentially overcome these weaknesses, and this study can be considered the first step toward this goal.

Before proxy data assimilation can be used, two significant technical issues must be overcome. The first is the utilization of time-averaged data. Because most of the proxy data currently being used is based on isotopes in

precipitation over a certain period, the information obtained is temporally averaged. The highest temporal resolution is at best monthly and can be obtained using cellulose ^{18}O or ice cores. Using time-averaged data for data assimilation is challenging although some progress has been made [Huntley and Hakim, 2010; Steiger *et al.*, 2014].

The second issue is the development of forward proxy models for each kind of proxy. IsoGCM produces information for isotopes in precipitation and most likely serves as a forward model for ice core isotopes from Greenland and Antarctica. However, for ice cap cores in locations such as the Andes or Alps, it may be necessary to create an additional forward model including the ablation and melting processes of snow. Similarly, for isotopic information in coral skeletons, cellulose, and speleothems new forward models are necessary to simulate the isotopic variations.

Even if these technical issues are overcome, an essential problem of proxy data assimilation would remain, i.e., the proxy information is simply too small to constrain the Earth system model. This might be the case, but a similar problem using reconstructed climate signals was considered by Mathiot *et al.* [2013]. They successfully performed simulations covering the early Holocene (10,000–8000 years ago) with a climate model of intermediate complexity that was constrained to follow the reconstructed temperature using a data assimilation method based on a particle filtering approach. In our case, it would be better to start with the near past (e.g., before the 19th century), with a particular focus on the last two millennia, when in situ measurement data of the atmosphere were much less available than they are now, so that the relative importance of the proxy is high. Furthermore, it is important to understand to what extent the Earth can be constrained using certain kinds of proxy data without using empirical relationships. This study is a first step toward this challenge.

5. Summary and Conclusions

In this study, we first developed a data-assimilation system using water vapor isotope information with an isotope-incorporated general circulation model (IsoGSM) and ensemble Kalman filter data assimilation scheme (LETKF). An observation system simulation experiment with synthetic but realistic observation data sets to represent a “perfect model” was performed to evaluate how the isotopic information could constrain the atmospheric dynamic fields. For the synthetic data sets, we mocked the spatiotemporal distributions of SCIAMACHY and TES retrievals and assumed a virtual network of in situ water vapor measurements on GNIP sites.

The 1-month test produced successful results overall. It confirmed that the inputted isotopic information could constrain not only the isotopic fields but also the atmospheric dynamic fields, such as air temperature, wind speed, humidity, and surface pressure. This was because vapor isotopic information is dependent on atmospheric transport (more specifically, an integrated record of condensation and evaporation), and constraining the isotopic fields would fix the influence of dynamic fields to some extent. The degree of improvement was basically proportional to the number of inputted data points, but with some arrangement in the horizontal and vertical location and timing of the measurement.

The results of this study can be applied in two directions. The first direction is a better analysis skill in current weather forecasting systems. Though our understanding of the atmosphere is improving, understanding the hydrological cycles of the mid- to upper troposphere and lower stratosphere in association with convective clouds remains difficult [Worden *et al.*, 2007; Frankenberg *et al.*, 2009; Schneider *et al.*, 2012]. Because it is apparent that water vapor isotopic information has unique characteristics with regard to the atmospheric hydrological cycle and technical improvements in satellite and in situ instruments are occurring rapidly, this direction is indeed quite promising.

The second direction, regarding proxy data assimilation, is even more challenging and is significant in several disciplines. In the past, we lacked direct measurements of the Earth and were forced to rely on proxy data. Interpretation of proxy data is important, but it is sometimes over-simplified. By using data assimilation for proxy data, an objective analysis of the past (specifically for the last two millennia, until the 19th century) can be achieved without simplifying the empirical relationship between proxy data and climate/environment information. Although there are many technical and theoretical obstacles in both directions, the authors strongly believe that scientific benefits can be achieved.

Acknowledgments

This study was conducted under the SOUSEI program and the SALSA/RECCA project of the Ministry of Education, Culture, Sports, Science, and Technology in Japan and the CREST program of Japan Science and Technology Agency. This research was also funded in part by the Japan Society for the Promotion of Science (JSPS) Grant 23686071, 23226012, and 26289160. The authors sincerely thank Junjie Liu at the JPL, Inez Fung at UC Berkeley, and Eugenia Kalnay at Maryland University for their help in the initial stage of this study. All of the data used in this study are available from the first author upon request.

References

- Alpert, J., M. Kanamitsu, P. Caplan, J. Sela, and G. White (1988), Mountain induced gravity wave drag parameterization in the NMC medium-range forecast model, in *Proceedings of Conference on 8th Numerical Weather Prediction*, pp. 726–733, Am. Meteorol. Soc., Baltimore, Md.
- Bishop, C. H., B. J. Etherton, and S. J. Majumdar (2001), Adaptive sampling with ensemble transform Kalman filter. Part I: Theoretical aspects, *Mon. Weather Rev.*, *129*, 420–436.
- Bowen, G. J. (2008), Spatial analysis of the intra-annual variation of precipitation isotope ratios and its climatological corollaries, *J. Geophys. Res.*, *113*, D05113, doi:10.1029/2007JD009295.
- Bowen, G. J., and J. Revenaugh (2003), Interpolating the isotopic composition of modern meteoric precipitation, *Water Resour. Res.*, *39*(10), 1299, doi:10.1029/2003WR002086.
- Cappa, C. D., M. B. Hendricks, D. J. DePaolo, and R. C. Cohen (2003), Isotopic fractionation of water during evaporation, *J. Geophys. Res.*, *108*(D16), 4525, doi:10.1029/2003JD003597.
- Chou, M.-D., and M. J. Suarez (1994), An efficient thermal infrared radiation parameterization for use in general circulation models, NASA Tech. Rep. TM-1994-104606 Series on Global Modeling and Data Assimilation, 85 pp.
- Craig, H., and L. Gordon (1965), Deuterium and oxygen-18 variations in the ocean and the marine atmosphere, in *Stable Isotopes in Oceanographic Studies and Paleotemperatures*, edited by E. Tongiorgi, pp. 9–130, Cons. Naz. di Rech., Spoleto, Italy.
- Dansgaard, W. (1964), Stable isotopes in precipitation, *Tellus*, *16*, 436–468.
- Ehhalt, D. H. (1974), Vertical profiles of HTO, HDO and H₂O in the troposphere, *Tech. Rep. NCAR-TN/STR-100*, Natl. Cent. for Atmos. Res., Boulder, Colo.
- Ek, M. B., K. E. Mitchell, Y. Lin, E. Rogers, P. Grunmann, V. Koren, G. Gayno, and J. D. Tarpley (2003), Implementation of Noah land surface model advances in the National Centers for Environmental Prediction operational mesoscale Eta model, *J. Geophys. Res.*, *108*(D22), 8851, doi:10.1029/2002JD003296.
- Farlin, J., C.-T. Lai, and K. Yoshimura (2013), Influence of synoptic weather events on the isotopic composition of atmospheric moisture in a coastal city of the western United States, *Water Resour. Res.*, *49*, 3685–3696, doi:10.1002/wrcr.20305.
- Frankenberg, C., et al. (2009), Dynamic processes governing the isotopic composition of water vapor as observed from space and ground, *Science*, *325*, 1374–1377, doi:10.1126/science.1173791.
- Frankenberg, C., D. Wunch, G. Toon, C. Risi, R. Scheepmaker, J.-E. Lee, P. Wennberg, and J. Worden (2013), Water vapor isotopologue retrievals from high-resolution GOSAT shortwave infrared spectra, *Atmos. Meas. Tech.*, *6*, 263–274, doi:10.5194/amt-6-263-2013.
- Gat, J. R. (2000), Atmospheric water balance—The isotopic perspective, *Hydrol. Processes*, *14*, 1357–1369.
- Gedzelman, S. D., and R. Arnold (1994), Modeling the isotopic composition of precipitation, *J. Geophys. Res.*, *99*, 10,455–10,471, doi:10.1029/93JD03518.
- Hoffmann, G., M. Werner, and M. Heimann (1998), The water isotope module of the ECHAM Atmospheric General Circulation Model – A study on timescales from days to several years, *J. Geophys. Res.*, *103*, 16,871–16,896, doi:10.1029/98JD00423.
- Hoffmann, G., J. Jouzel, and V. Masson (2000), Stable water isotopes in atmospheric general circulation models, *Hydrol. Processes*, *14*, 1385–1406.
- Hong, S.-Y., and H.-L. Pan (1998), Convective trigger function for a mass flux cumulus parameterization scheme, *Mon. Weather Rev.*, *126*, 2599–2620.
- Hunt, B. R., E. Kalnay, E. J. Kostelich, E. Ott, D. J. Patil, T. Sauer, I. Szunyogh, J. A. Yorke, and A. V. Zimin (2004), Four-dimensional ensemble Kalman filtering, *Tellus A*, *56*, 273–277.
- Hunt, B., E. Kostelich, and I. Szunyogh (2007), Efficient data assimilation for spatiotemporal chaos: A local ensemble transform Kalman filter, *Phys. D*, *230*, 112–126.
- Huntley, H. S., and G. J. Hakim (2010), Assimilation of time-averaged observations in a quasi-geostrophic atmospheric jet model, *Clim. Dyn.*, *35*, 995–1009.
- International Atomic Energy Agency (2001), The global network of isotopes in precipitation. [Available at <http://isohis.iaea.org/>]
- Ishizaki, Y., K. Yoshimura, S. Kanae, M. Kimoto, N. Kurita, and T. Oki (2012), Interannual variability of H₂¹⁸O in precipitation over the Asian monsoon region, *J. Geophys. Res.*, *117*, D16308, doi:10.1029/2011JD015890.
- Joussame, S., R. Sadourny, and J. Jouzel (1984), A general circulation model of water isotope cycles in the atmosphere, *Nature*, *311*, 24–29.
- Jouzel, J. (1986), Isotopes in cloud physics: Multiphase and multistage condensation processes, in *Handbook of Environmental Isotope Geochemistry*, vol. 2, edited by P. Fritz and J. C. Fontes, pp. 61–112, Elsevier, New York.
- Jouzel, J., and L. Merlivat (1984), Deuterium and oxygen 18 in precipitation: Modeling of the isotopic effects during snow formation, *J. Geophys. Res.*, *87*, 11,749–11,757, doi:10.1029/JD089iD07p11749.
- Jouzel, J., G. L. Russell, R. J. Suozzo, R. D. Koster, J. W. C. White, and W. S. Broecker (1987), Simulations of HDO and H₂¹⁸O atmospheric cycles using the NASA GISS general circulation model: The seasonal cycle for present-day conditions, *J. Geophys. Res.*, *92*, 14,739–14,760, doi:10.1029/JD092iD12p14739.
- Kalnay, E., L. Hong, T. Miyoshi, S.-C. Yang, and J. Ballabrera-Poy (2007), 4D-Var or ensemble Kalman filter?, *Tellus A*, *59*, 758–773.
- Kanamitsu, M., et al. (2002a), NCEP dynamical seasonal forecast system 2000, *Bull. Am. Meteorol. Soc.*, *83*, 1019–1037.
- Kanamitsu, M., W. Ebisuzaki, J. Woolen, J. Potter, and M. Fiorino (2002b), NCEP/DOE AMIP-II Reanalysis (R-2), *Bull. Am. Meteorol. Soc.*, *83*, 1631–1643.
- Kang, J.-S., E. Kalnay, J. Liu, I. Fung, T. Miyoshi, and K. Ide (2011), “Variable localization” in an ensemble Kalman filter: Application to the carbon cycle data assimilation, *J. Geophys. Res.*, *116*, D09110, doi:10.1029/2010JD014673.
- Kang, J.-S., E. Kalnay, T. Miyoshi, J. Liu, and I. Fung (2012), Estimation of surface carbon fluxes with an advanced data assimilation methodology, *J. Geophys. Res.*, *117*, D24101, doi:10.1029/2012JD018259.
- Lacour, J.-L., C. Risi, L. Clarisse, S. Bony, D. Hurtmans, C. Clerbaux, and P.-F. Coheur (2012), Mid-tropospheric δD observations from IASI/MetOp at high spatial and temporal resolution, *Atmos. Chem. Phys.*, *12*, 10,817–10,832, doi:10.5194/acp-12-10817-2012.
- Lee, J.-E., I. Fung, D. J. DePaolo, and C. C. Henning (2007), Analysis of the global distribution of water isotopes using the NCAR atmospheric general circulation model, *J. Geophys. Res.*, *112*, D16306, doi:10.1029/2006JD007657.
- Lee, J.-E., I. Fung, C. Risi, J. Worden, R. Scheepmaker, and C. Frankenberg (2012), Asian monsoon hydrology from LMDZ GCM and two satellite measurements (TES and SCIAMACHY) of water vapor isotopes: implications for speleothem data interpretation, *J. Geophys. Res.*, *117*, D15112, doi:10.1029/2011JD017133.
- Lee, J.-H., J. Worden, D.-C. Koh, K. Yoshimura, and J.-E. Lee (2013), A seasonality of δD of water vapor (850–500 hPa) observed from space over Jeju island, Korea, *Geosci. J.*, *17*, 87–95, doi:10.1007/s12303-013-0003-5.
- Majoube, M. (1971a), Oxygen-18 and deuterium fractionation between water and steam [in French], *J. Chim. Phys. Phys. Chim. Biol.*, *68*, 1423–1436.
- Majoube, M. (1971b), Fractionation in O-18 between ice and water vapor [in French], *J. Chim. Phys. Phys. Chim. Biol.*, *68*, 625–636.

- Mathieu, R., D. Pollard, J. E. Cole, J. W. C. White, R. S. Webb, and S. L. Thompson (2002), Simulation of stable water isotope variations by the GENESIS GCM for modern conditions, *J. Geophys. Res.*, *107*(D4), 4037, doi:10.1029/2001JD900255.
- Mathiot, P., H. Goosse, X. Crosta, B. Stenni, M. Braida, H. Renssen, C. J. Van Meerbeek, V. Masson-Delmotte, A. Mairesse, and S. Dubinkina (2013), Using data assimilation to investigate the causes of Southern Hemisphere high latitude cooling from 10 to 8 ka BP, *Clim. Past*, *9*, 887–901.
- Merlivat, L. (1978), Molecular diffusivities of H_2^{16}O , HD^{16}O and H_2^{18}O in gases, *J. Chim. Phys.*, *69*, 2864–2871.
- Merlivat, L., and J. Jouzel (1979), Global climatic interpretation of the deuterium oxygen 18 relationship for precipitation, *J. Geophys. Res.*, *84*, 5029–5033, doi:10.1029/JC084iC08p05029.
- Miyoshi, T. (2011), The Gaussian approach to adaptive covariance inflation and its implementation with the local ensemble transform Kalman filter, *Mon. Weather Rev.*, *139*, 1519–1535.
- Miyoshi, T., and S. Yamane (2007), Local ensemble transform Kalman filtering with an AGCM at T159/L60 resolution, *Mon. Weather Rev.*, *135*, 3841–3861.
- Moorthi, S., and M. J. Suarez (1992), Relaxed Arakawa-Schubert: A parameterization of moist convection for general circulation models, *Mon. Weather Rev.*, *120*, 978–1002.
- Noone, D., and I. Simmonds (2002), Associations between d^{18}O of water and climate parameters in a simulation of atmospheric circulation 1979–1995, *J. Clim.*, *15*, 3150–3169.
- Ott, E., B. R. Hunt, I. Szunyogh, A. V. Zimin, E. J. Kostelich, M. Corazza, E. Kalnay, D. J. Patil, and J. A. Yorke (2002), Exploiting local low dimensionality of the atmospheric dynamics for efficient Kalman filtering, *ArXiv*, arc-ive/paper 0203058. [Available at <http://arxiv.org/abs/physics/020358>.]
- Ott, E., et al. (2004), A local ensemble Kalman filter for atmospheric data assimilation, *Tellus A*, *56*, 415–428.
- Parrish, D. F., and J. C. Derber (1992), The National Meteorological Center's Spectral Statistical-Interpolation Analysis System, *Mon. Weather Rev.*, *120*, 1747–1763.
- Payne, V. H., D. Noone, A. Dudhia, C. Piccolo, and R. G. Grainger (2007), Global satellite measurements of HDO and implications for understanding the transport of water vapour into the stratosphere, *Q. J. R. Meteorol. Soc.*, *133*, 1459–1471.
- Risi, C., S. Bony, F. Vimeux, and J. Jouzel (2010), Water stable isotopes in the LMDZ4 General Circulation Model: Model evaluation for present day and past climates and applications to climatic interpretation of tropical isotopic records, *J. Geophys. Res.*, *115*, D12118, doi:10.1029/2009JD013255.
- Risi, C., et al. (2012a), Process-evaluation of tropospheric humidity simulated by general circulation models using water vapor isotopologues. Part 1: Comparison between models and observations, *J. Geophys. Res.*, *117*, D05303, doi:10.1029/2011JD016621.
- Risi, C., et al. (2012b), Process-evaluation of tropospheric humidity simulated by general circulation models using water vapor isotopic observations. Part 2: Using isotopic diagnostics to understand the mid and upper tropospheric moist bias in the tropics and subtropics, *J. Geophys. Res.*, *117*, D05304, doi:10.1029/2011JD016623.
- Schmidt, G. A., G. Hoffmann, D. T. Shindell, and Y. Hu (2005), Modeling atmospheric stable water isotopes and the potential for constraining cloud processes and stratosphere-troposphere water exchange, *J. Geophys. Res.*, *110*, D21314, doi:10.1029/2005JD005790.
- Schneider, M., et al. (2012), Ground-based remote sensing of tropospheric water vapour isotopologues within the project MUSICA, *Atmos. Meas. Tech.*, *5*, 3007–3027, doi:10.5194/amt-5-3007-2012.
- Steiger, N. J., G. J. Hakim, E. J. Steig, D. S. Battisti, and G. H. Roe (2014), Assimilation of time-averaged pseudoproxies for climate reconstruction, *J. Clim.*, *27*, 426–441.
- Stewart, M. K. (1975), Stable isotope fractionation due to evaporation and isotopic exchange of falling waterdrops: Applications to atmospheric processes and evaporation of lakes, *J. Geophys. Res.*, *80*, 1138–1146, doi:10.1029/JC080i009p01133.
- Tiedtke, M. (1983), The sensitivity of the time-mean large-scale flow to cumulus convection in the ECMWF model, in *Proc. Workshop on Convection in Large-Scale Numerical Models*, Reading, pp. 297–316, ECMWF, U. K.
- Tindall, J. C., P. J. Valdes, and L. C. Sime (2009), Stable water isotopes in HadCM3: Isotopic signature of El Niño–Southern Oscillation and the tropical amount effect, *J. Geophys. Res.*, *114*, D04111, doi:10.1029/2008JD010825.
- Uemura, R., Y. Matsui, K. Yoshimura, H. Motoyama, and N. Yoshida (2008), Evidence of deuterium excess in water vapour as an indicator of ocean surface conditions, *J. Geophys. Res.*, *113*, D19114, doi:10.1029/2008JD010209.
- Uemura, R., N. Yonezawa, K. Yoshimura, R. Asami, H. Kadena, K. Yamada, and N. Yoshida (2012), Factors controlling isotopic composition of precipitation on Okinawa Island, Japan: Implications for paleoclimate reconstruction in the East Asian Monsoon region, *J. Hydrol.*, *475*, 314–322.
- Webster, C. R., and A. J. Heymsfield (2003), Water isotope ratios D/H, 18O/16O, 17O/16O in and out of clouds map dehydration pathways, *Science*, *302*, 1742–1745.
- Whitaker, J. S., T. M. Hamill, X. Wei, Y. Song, and Z. Toth (2008), Ensemble data assimilation with the NCEP global forecast system, *Mon. Weather Rev.*, *136*, 463–482.
- Worden, J., et al. (2006), Tropospheric Emission Spectrometer observations of the tropospheric HDO/H₂O ratio: Estimation approach and characterization, *J. Geophys. Res.*, *111*, D16309, doi:10.1029/2005JD006606.
- Worden, J., D. Noone, and K. Bowman (2007), Importance of rain evaporation and continental convection in the tropical water cycle, *Nature*, *445*, doi:10.1038/nature05508.
- Yoshimura, K., and M. Kanamitsu (2008), Dynamical global downscaling of global reanalysis, *Mon. Weather Rev.*, *136*(8), 2983–2998.
- Yoshimura, K., T. Oki, N. Ohte, and S. Kanae (2003), A quantitative analysis of short-term ^{18}O variability with a Rayleigh-type isotope circulation model, *J. Geophys. Res.*, *108*(D20), 4647, doi:10.1029/2003JD003477.
- Yoshimura, K., T. Oki, and K. Ichiyonagi (2004), Evaluation of two-dimensional atmospheric water circulation fields in reanalyses by using precipitation isotopes databases, *J. Geophys. Res.*, *109*, D20109, doi:10.1029/2004JD004764.
- Yoshimura, K., S. Miyazaki, S. Kanae, and T. Oki (2006), Iso-MATSIRO, a land surface model that incorporates stable water isotopes, *Global Planet. Change*, *51*, 90–107.
- Yoshimura, K., M. Kanamitsu, D. Noone, and T. Oki (2008), Historical isotope simulation using reanalysis atmospheric data, *J. Geophys. Res.*, *113*, D19108, doi:10.1029/2008JD010074.
- Yoshimura, K., M. Kanamitsu, and M. Dettlinger (2010), Regional downscaling for stable water isotopes: A case study of an Atmospheric River event, *J. Geophys. Res.*, *115*, D18114, doi:10.1029/2010JD014032.
- Yoshimura, K., C. Frankenberg, J. Lee, M. Kanamitsu, J. Worden, and T. Röckmann (2011), Comparison of an isotopic AGCM with new quasi global satellite measurements of water vapor isotopologues, *J. Geophys. Res.*, *116*, D19118, doi:10.1029/2011JD016035.
- Zakharov, V. I., R. Imasu, K. G. Gribanov, G. Hoffmann, and J. Jouzel (2004), Latitudinal distribution of the deuterium to hydrogen ratio in the atmosphere water vapor retrieved from IMG/ADEOS data, *Geophys. Res. Lett.*, *31*, L12104, doi:10.1029/2004GL019433.
- Zhu, M., L. D. Stott, B. Buckley, K. Yoshimura, and K. Ra (2012), Indo-Pacific Warm Pool convection and ENSO since 1867 AD derived from Cambodian pine tree cellulose oxygen isotopes, *J. Geophys. Res.*, *117*, D11307, doi:10.1029/2011JD017198.